On the origin of topotactic reduction effect for superconductivity in infinite-layer nickelates

Shengwei Zeng[1, #,*], Chi Sin Tang[2,3, #,*], Zhaoyang Luo[2, #], Lin Er Chow[2], Zhi Shiuh Lim[1], Saurav Prakash[2], Ping Yang[3], Caozheng Diao[3], Xiaojiang Yu[3], Zhenxiang Xing[1], Rong Ji[1] , Xinmao Yin,[4] Changjian Li[5], X. Renshaw Wang[6], Qian He[7], Mark B. H. Breese[2,3], A. Ariando[2,*], Huajun Liu[1,*]

[1]*Institute of Materials Research and Engineering (IMRE), Agency for Science, Technology and Research (A*STAR), 2 Fusionopolis Way, Innovis #08-03, Singapore 138634, Republic of Singapore.*

[2]*Department of Physics, Faculty of Science, National University of Singapore, Singapore 117551, Republic of Singapore.*

[3]*Singapore Synchrotron Light Source (SSLS), National University of Singapore, 5 Research Link, Singapore 117603, Republic of Singapore.*

[4]*Shanghai Key Laboratory of High Temperature Superconductors, Physics Department, Shanghai University, Shanghai 200444, China.*

[5]*Department of Materials Science and Engineering, Southern University of Science and Technology, Shenzhen 518055, Guangdong, China.*

[6]*Division of Physics and Applied Physics, School of Physical and Mathematical Sciences, Nanyang Technological University, Singapore 637371, Republic of Singapore.*

[7]*Department of Materials Science and Engineering, National University of Singapore, Singapore 117575, Republic of Singapore.*

[#]The authors contributed equally to this work.

*To whom correspondence should be addressed.

E-mail: zeng_shengwei@imre.a-star.edu.sg; slscst@nus.edu.sg; ariando@nus.edu.sg; liu_huajun@imre.a-star.edu.sg

Topotactic reduction utilizing metal hydrides as reagents emerges as an effective approach to achieve exceptionally low oxidization states of metal ions and unconventional coordination networks. This method opens avenues to the development of entirely new functional materials, with one notable example being the infinite-layer nickelate superconductors. However, the reduction effect on the atomic reconstruction and electronic structures – crucial for superconductivity – remains largely unresolved. We design two sets of control $Nd_{0.8}Sr_{0.2}NiO_2$ thin films and implement secondary ion mass spectroscopy to highlight the absence of reduction-induced hydrogen intercalation. X-ray absorption spectroscopy shows a significant linear dichroism with dominant Ni $3d_{x2-y2}$ orbitals on superconducting samples, indicating a Ni single-band nature of infinite-layer nickelates. Consistent with the superconducting T_c, the Ni 3*d* orbitals asymmetry manifests a dome-like reduction duration dependence. Our results unveil the critical role of reduction in modulating the Ni-3*d* orbital polarization and its impact on the superconducting properties.

The discovery of superconductivity in infinite-layer nickelate $(La/Pr/Nd)_{1-x}(Sr/Ca)_xNiO_2$ thin films has stimulated intensive interests owing to its scientific richness in understanding the mechanism of high-T_c superconductivity [1-7]. Subsequent observations of pressure- and strain-induced T_c enhancement in infinite-layer films [8-10], superconductivity in quintuple-layer nickelate $Nd_6Ni_5O_{12}$ (ref. [11]), and T_c near 80 K in bilayer compounds $La_3Ni_2O_7$ (ref. [12]) further suggest nickelates as an alternatively promising route towards high-T_c superconductors. Even though it is resemblant to high-T_c cuprates in $3d^9$ electron configuration and layered crystal structure, the infinite-layer nickelates showed different features such as Mott-Hubbard scenario in band structure [13-15], absence of long-range antiferromagnetic order [16-18], complexed paring symmetry [5, 19-22]. Even for samples with the same chemical composition, the experimental characterization of electronic structure such as the charge density wave is controversial [23-26]. Furthermore, bulk materials showed absence of superconductivity despite the presence of infinite-layer phase [27, 28]. Such disputable observations could be attributed to the challenging material synthesis and topotactic reduction process [29].

The infinite-layer nickelates are realized by the CaH_2-facilitated reduction from perovskite precursors, during which atomic reconstruction/element intercalation may occur and significantly modify the electronic structures [30]. A notable effect of reduction has been recently reported to be hydrogen (H) intercalation (H is from the reagent CaH_2), showing a critical role for superconductivity in $Nd_{0.8}Sr_{0.2}NiO_2H_x$, with zero resistivity only found in a very narrow H-concentration window [31]. However, the theoretical calculation showed that H intercalation resulted in Ni $3d^8$ configuration with mixed $3d_{x2-y2}$ and $3d_{z2}$ orbitals at Fermi level [32], even though single $3d_{x2-y2}$ is possible at certain H concentration of 25% (ref. [33]). The electron-phonon coupling involved with H doping was also suggested to be too weak to

support the observed T_c (ref. [34]). Moreover, superconductivity in $Nd_{1-x}Eu_xNiO_2$ films have been achieved through in-situ reduction using metallic aluminium where the hydrogen source is absent [35]. Furthermore, the presence of defects such as Ruddlesden–Popper-type faults may cause moisture absorption at defect boundary and controversial characterization of H intercalation [2, 4, 29]. Therefore, it is desirable to clarify the reduction effect on atomic reconstruction and electronic structure, and the role leading to superconductivity in pure infinite-layer nickelates. Here we design two sets of nickelate samples and perform the ion mass spectrometry and X-ray absorption spectroscopy to reveal the role of reduction effect. The first set is 5-nm pure infinite-layer $Nd_{0.8}Sr_{0.2}NiO_2$ film capped by 5-nm $SrTiO_3$ as a protection layer (**referred as STO/NSNO**) and the other set is 20-nm thicker film with mixed phases (**referred as tNSNO**).

The sample preparation is the same as described in our previous reports [4, 7]. The nickelate films and STO capping layers were grown on TiO_2-terminated STO (001) substrates by pulsed laser deposition (PLD), at temperature of 600 ^oC and oxygen partial pressure of 150 mTorr. After deposition, the as-grown samples were reduced at 340 ^oC for different duration using CaH_2 as reagent. The electrical transport was measured using a Quantum Design PPMS. The X-ray diffraction (XRD) was measured in X-ray Diffraction and Development beamline at Singapore Synchrotron Light Source (SSLS). The X-ray absorption spectroscopy (XAS) was measured using linearly polarized X-ray from the Soft X-Ray—Ultraviolet (SUV) beamline and the Surface, Interface, and Nanostructure Science (SINS) beamline at SSLS. A total electron yield (TEY) detection method is used during the measurements. The high-angle annular dark-field scanning transmission electron microscopy (HAADF-STEM) imaging was carried out using

a JEOL ARM200F microscope. The element depth profiles were measured using Time-of-flight secondary ion mass spectrometry (TOF-SIMS). The detailed thin film preparation and measurements can be seen in Method Section of Supplementary Materials [36].

Figure 1(a) shows the HAADF-STEM image of the optimally reduced STO/NSNO. A clear infinite-layer structure is observed with no obvious defect throughout the layer, confirming high crystalline quality. However, a defect area, which is widely distributed throughout the top area of nickelate layer, is clearly observed for the over-reduced sample (Fig. 1(b)). In the defect area, a stripe feature is manifested with additional atoms between two Nd atom planes. These could be the interstitial Ni/Nd atoms which take the position of original oxygen in NiO_2 plane (Fig. 1(c)). The formation of interstitial atoms could be related to the creation of oxygen vacancies in NiO_2 plane induced during the over-reduction process, and therefore, the neighbouring Nd or Ni atoms drift into the vacancy sites. With increasing reduction time, the *c*-axis lattice constants, denoted as *c,* calculated from XRD scans, decrease and reach a minimum value of ~3.331 Å, before increasing with longer reduction times (Fig. 4). The increase of *c* at longer duration is due to the presence of more oxygen vacancies and interstitial Ni/Nd. For tNSNO samples, a similar trend is seen with smallest *c* at 80 min and larger *c* at longer reduction (Supplementary Materials Fig. S1) [36]. In contrast to pure infinite-layer phase in STO/NSNO, defects with Ruddlesden–Popper-type secondary phase is seen at the top section of the tNSNO film [2, 4, 29] (Supplementary Materials Fig. S1) [36].

Figure 1(d) shows the resistivity *versus* temperature (*ρ*-*T*) curves of STO/NSNO at different reduction time. The films reduced for 40 and 50 mins show insulating behaviour (the

resistance is out of measurement limit for 40 mins). By increasing reduction time to 80-360 mins, the samples become superconducting with ρ-T curves showing metallic behaviour at high temperature. Sharp superconducting transition and the highest critical temperature, T_c, are achieved at 80 and 180 mins (see also Fig. 4). By further increasing the reduction time to 720 mins, the sample becomes weakly insulating at low temperature, which is similar the over-doped infinite-layer nickelates [2-4, 6, 7]. The reduction effect on T_c is summarized as a phase diagram in Fig. 4. The phase diagram can be separated to under-reduced (insulating), optimally reduced (superconducting with highest T_c) and over-reduced (superconducting with lower T_c and weekly insulating) regions. For tNSNO samples, the reduction shows a similar effect with a superconducting transition for 80 mins and a weakly insulating behaviour for 720 mins (Fig. 1(e)). The normal-state Hall coefficients (R_H) of STO/NSNO shows a change from negative to positive signs at low temperature for optimally reduced samples [1, 2, 4], while it remains negative for under- and over-reduced samples (Fig. 1(f)). The reduction duration dependence of the R_H at 20 K and 300 K is plotted in Fig. 1(g), clearly showing a sign change with increasing reduction time.

Figures 2(a) and 2(b) show the TOF-SIMS signals of H profile for bare STO substrate, STO/NSNO and tNSNO. The Ni, Ti and Nd profiles of STO/NSNO and tNSNO at a reduction time of 80 mins are plotted in Fig. 2(c) and 2(d), respectively, clearly indicating the well-defined layer structures between nickelate and STO. The three-dimensional (3D) mappings show that the elements of the nickelate film are uniformly distributed with no chemical segregation (Fig. 2(e)). Other SIMS data are shown in Supplementary Materials Fig. S2 and Fig. S3 [36]. With STO capping, the as-grown and reduced STO/NSNO show comparable H signal intensity with

exception for the surface and interface. Moreover, the difference in H intensity between the nickelate and the background of STO substrates is not obvious. This is in contrast to previous observation in reference [31], where the H intensity in $Nd_{0.8}Sr_{0.2}NiO_2$ films is two orders of magnitude higher than that in STO. For comparison, we also performed TOF-SIMS measurements on tNSNO (Fig. 2(b)). For tNSNO, the pure infinite-layer structure with thickness up to ~10 nm could be achieved at the bottom area of the film near STO substrate, whereas the top area above ~10 nm consists of mixed phases [2, 4, 29] (Supplementary Materials Fig. S1). One can see that the H intensity is higher on the surface, and gradually decreases into the film. At the bottom of the film (sputtering time from 200 to 400 sec), the intensity is comparable to that of the STO/NSNO sample and STO substrates. We also plot the H relative intensity compared to the substrate background for both STO/NSNO and *t*NSNO samples in Supplementary Materials Fig. S4, demonstrating similar H intensity between the as-grown and reduced samples. Overall, the low H intensity in STO/NSNO and bottom area of tNSNO reduced over a wide range of durations indicate that the reduction-induced H intercalation in pure infinite-layer phase is negligible. In contrast, higher H intensity at the top area of tNSNO possibly indicate the moisture absorption due to the presence of defects.

It is worth noting that reduction-induced H intercalation was reported to be in $NdNiO_xH_y$ film with defect-fluorite structure, while H is absent in infinite-layer phase [37]. Moreover, no hydrogen in $LaNiO_2$ polycrystalline powder was detected using neutron diffraction, and the extra hydrogen might be confined to polycrystalline grain boundaries or secondary-phase precipitate [38]. Reduction-induced H intercalation was reported in other perovskites such as $SrVO_x$ (ref. [30, 39]). However, the reduction temperature (~ 600 ^oC) and duration (~ 24 hours)

required for topotactic transition in $SrVO_x$ is much higher and longer, compared to those for nickelates (240-340 ^oC and several hours) [30]. Moreover, the reduction process was usually conducted in a small and sealed quartz tube. This differs from our method wherein the reduction process is performed in a large vacuum chamber [30-31]. The confined space of the former study resulted in a high vapor partial pressure within the quartz tube, where H_2O is a by-product of the reduction reaction and is released from the reagent. This may in turn lead to an absorption of vapor within the nickelate thin films. Therefore, to avoid H intercalation, it is desirable to use a precursor with a pure perovskite phase, employ a lower reduction temperature, and control vapor partial pressure appropriately.

Having deduced that the H intercalation is negligible, we then investigate the effects of reduction on the nickelate electronic structures. Figure 3(a) shows an example of Ni $L_{2,3}$ edge XAS of STO/NSNO reduced for 180 mins where the spectra are taken at incident angles of 20^o ($\varepsilon \perp a$, ε indicates electric field and a indicates the NiO_2 plane) and 90^o ($\varepsilon // a$). The dominant absorption peaks at ~853 eV and ~870 eV are clearly observed, corresponding to the $2p^6{}_{3/2}3d^9 \Rightarrow 2p^5{}_{3/2}3d^{10}$ and $2p^6{}_{1/2}3d^9 \Rightarrow 2p^5{}_{1/2}3d^{10}$ transitions, respectively [40]. The light polarization effect shows a significant linear dichroism with a larger absorption as ε is aligned in-plane, as compared to that when ε is aligned out-of-plane. The Ni $L_{2,3}$ edges XAS for other STO/NSNO samples are plotted together in Supplementary Materials Fig. S5 [36]. The spectra linear dichroism, $\Delta I = I(\varepsilon // a) - I(\varepsilon \perp a)$, are shown in Fig. 3(b) where the Ni-L_3 peak dichroism are plotted with respect to the reduction duration in the inset of Fig. 3(b). For the sample reduced for 40 mins, there is a slight linear dichroism. As the reduction duration increases, there is a corresponding increase in ΔI and it maximizes at 180 mins. Beyond which, the ΔI decreases as

the samples are over-reduced. To further characterize the linear dichroism, the Ni-L_3 peak asymmetry percentage, $\Delta I\% = [I(\varepsilon /\!/ a) - I(\varepsilon \perp a)] / [I(\varepsilon /\!/ a) + I(\varepsilon \perp a)]$, is plotted as a function of reduction duration in Fig. 4. The orbital asymmetry shows a large tunability by reduction with a range from 5.5 to 69.1%. In addition, the asymmetry shows a dome-shape behaviour with respect to the reduction time, which is consistent with the change of T_c.

The clear correlation between the XLD and reduction duration is a strong indication that the reduction process has a direct impact on the Ni 3*d* orbital polarization, and this in turn is critical to the superconducting properties of the infinite-layer nickelates. According to the crystal field configuration, the energy level of Ni $3d_{z2}$ orbital is lowered to be comparable to that of the t_{2g} orbitals under NiO_2 square planar coordination, and therefore, $3d_{x2-y2}$ orbital becomes isolated from other 3*d* orbitals [41]. The optimally reduced condition enables the realization of this perfect square planar field, leading to a single Ni $3d_{x2-y2}$ band with two-dimensional nature which favours the occurrence of superconductivity [41, 42]. This is consistent with the smallest *c*-axis lattice constant and the largest orbital asymmetry at the optimally reduced region (Fig. 4 and Supplementary Materials Fig. S6) [36]. In the under-reduced condition, with the incomplete transition to the infinite-layer structure, residual apical oxygens with a shorter Ni-O apical distance are present [43]. This results in the lifting of $3d_{z2}$ level and the resultant admixing of the $3d_{x2-y2}$ and $3d_{z2}$ orbitals. The doped holes and unoccupied states reside in this mixed band and thus, orbital asymmetry is small. In the over-reduced condition, the creation of oxygen vacancies in NiO_2 plane and the resultant formation of interstitial Ni/Nd atoms lead to deviation of the Ni-coordination from the long range-order planar square configuration. Likewise, this structural deviation results in the hybridization of

the $3d_{x2-y2}$ and $3d_{z2}$ orbitals. Hence, in both the under- and over-reduced conditions, the presence of residual apical oxygen and interstitial atoms in NiO_2 planes have detrimental effects on the realization of superconductivity due to the hybridization effects of both the $3d_{x2-y2}$ and $3d_{z2}$ orbitals. The weakening of single-band feature due to residual apical oxygen and its detrimental effect to superconductivity have also been demonstrated at the $NdNiO_2$/STO interfaces [41, 44-46].

The reduction effect on orbital polarization is consistent with the observation that multiband structures become more pronounced in the under- and over-reduced regimes. As shown in Fig. 1(f) and 1(g), R_H remains negative in under- and over-reduced regimes while there is a change in sign in optimally reduced regime. It should be noted that the multiband structures may originate from the rare-earth element $5d_{xy}$ and $5d_{z2}$ orbitals, and the reduction effect on these orbitals is worthy of further investigation [41, 47]. With respect to infinite-layer nickelate bulks, superconductivity is absent even though that the perfect diamagnetism and high critical current density measured on thin film indicate the bulk nature of superconductivity [1, 48]. In bulk materials, the reduction duration required to obtain the infinite-layer structure is more than 20 hours [27, 28, 49]. Such prolonged reduction makes it vulnerable to the formation of in-plane oxygen vacancies and interstitial atoms, which may be the reason for absence of superconductivity in the bulk form [27, 28, 49].

In summary, we highlight that CaH_2 reduction-induced H intercalation is negligible in pure infinite-layer phase, thus not critical to superconductivity. The reduction significantly influences the Ni 3*d* orbital polarization with dominant $3d_{x2-y2}$ orbital in optimally reduced

condition, which is critical for the realization of superconductivity in infinite-layer nickelates. The reduction-induced residual apical oxygen, in-pane oxygen vacancies and interstitial Ni/Nd atoms weaken the Ni planar square configuration, resulting in a consistent dome-shape diagram for both T_c and Ni 3*d* orbital asymmetry.

Acknowledgments

S.W.Z., Z.S.L., and H.J.L. acknowledge the RIE2025 MTC Individual Research Grants (M22K2c0084), National Research Foundation Competitive Research Program (NRF-CRP28-2022-0002), Career Development Fund (C210812020) and Central Research Fund from the Agency for Science, Technology and Research (A*STAR) for the funding support. The work at NUS and the authors are supported by the Ministry of Education (MOE), Singapore, under its Tier-2 Academic Research Fund (AcRF) (Grants No. MOE-T2EP50121-0018 and MOE T2EP50123-0013) and the National Research Foundation (NRF) of Singapore under its NRF-ISF joint program (Grant no. NRF2020-NRF-ISF004-3518). X.R.W. acknowledges support from Singapore Ministry of Education under its Academic Research Fund (AcRF) Tier 2 (Grant No. MOE-T2EP50120-0006). X.M.Y. acknowledges financial support by National Natural Science Foundation of China (Grant No.12374378). C.S.T acknowledges the support from the NUS Emerging Scientist Fellowship. The authors would like to acknowledge the Singapore Synchrotron Light Source for providing the facility necessary for conducting the research. The Laboratory is a National Research Infrastructure under the National Research Foundation, Singapore. Any opinions, findings, and conclusions or recommendations expressed in this

material are those of the author(s) and do not reflect the views of National Research Foundation, Singapore.

Author contributions

S.W.Z., H.J.L., A.A., C.S.T. and Z.Y.L. conceived the main idea. S.W.Z., Z.Y.L., L.E.C., Z.S.L. and S.P. prepared the thin films and conducted the electrical measurements. C.S.T., S.W.Z. and P.Y. conducted the XRD measurements. C.S.T., C.Z.D., X. J. Y. and M.B.H.B. conducted the XAS measurements. Z.Y.L., Q. H. and C.J.L. conducted the STEM measurements. Z.X.X. and R.J. conducted the TOF-SIMS measurements. X.M.Y., C.J.L. and X.R.W. provide insight to manuscript. S.W.Z., H.J.L., A.A., C.S.T. and Z.Y.L. wrote the manuscript with contributions from all authors. All authors have discussed the results and the interpretations.

Competing interests

The authors declare no competing interests.

References

[1] D. Li, K. Lee, B. Y. Wang, M. Osada, S. Crossley, H. R. Lee, Y. Cui, Y. Hikita, and H. Y. Hwang, Nature **572**, 624 (2019).

[2] D. Li, B. Y. Wang, K. Lee, S. P. Harvey, M. Osada, B. H. Goodge, L. F. Kourkoutis, and H. Y. Hwang, Phys. Rev. Lett. **125**, 027001 (2020).

[3] M. Osada, B. Y. Wang, K. Lee, D. Li, and H. Y. Hwang, Phys. Rev. Mater. **4**, 121801 (2020).

[4] S. Zeng, C. S. Tang, X. Yin, C. Li, M. Li, Z. Huang, J. Hu, W. Liu, G. J. Omar, H. Jani, Z. S. Lim, K. Han, D. Wan, P. Yang, S. J. Pennycook, A. T. S. Wee, and A. Ariando, Phys. Rev. Lett. **125**, 147003 (2020).

[5] Q. Gu, Y. Li, S. Wan, H. Li, W. Guo, H. Yang, Q. Li, X. Zhu, X. Pan, Y. Nie, and H. H. Wen, Nat. Commun. **11**, 6027 (2020).

[6] M. Osada, B. Y. Wang, B. H. Goodge, S. P. Harvey, K. Lee, D. Li, L. F. Kourkoutis, and H. Y. Hwang, Adv. Mater. **33**, 2104083 (2021).

[7] S. Zeng, C. Li, L. E. Chow, Y. Cao, Z. Zhang, C. S. Tang, X. Yin, Z. S. Lim, J. Hu, P. Yang, and A. Ariando, Sci. Adv. **8**, eabl9927 (2022).

[8] N. Wang, M. Yang, Z. Yang, K. Chen, H. Zhang, Q. Zhang, Z. Zhu, Y. Uwatoko, L. Gu, X. Dong, J. Sun, K. Jin and J. Cheng, Nat. Commun. **13**, 4367 (2022).

[9] K. Lee, B.Y. Wang, M. Osada, B.H. Goodge, T.C. Wang, Y. Lee, S. Harvey, W. J. Kim, Y. Yu, C. Murthy, S. Raghu, L. F. Kourkoutis and H. Y. Hwang, Nature **619**, 288-292 (2023).

[10] X. Ren, J. Li, W.-C. Chen, Q. Gao, J. J. Sanchez, J. Hales, H. Luo, F. Rodolakis, J. L. McChesney, T. Xiang, J. Hu, R. Comin, Y. Wang, X. Zhou, and Z. Zhu, Commun. Phys. **6**, 341 (2023).

[11] G. A. Pan, D. Ferenc Segedin, H. LaBollita, Q. Song, E. M. Nica, B. H. Goodge, A. T. Pierce, S. Doyle, S. Novakov, D. Córdova Carrizales, A. T. N'Diaye, P. Shafer, H. Paik, J. T. Heron, J. A. Mason, A. Yacoby, L. F. Kourkoutis, O. Erten, C. M. Brooks, A. S. Botana, and J. A. Mundy, Nat. Mater. **21**, 160-164 (2022).

[12] H. Sun, M. Huo, X. Hu, J. Li, Z. Liu, Y. Han, L. Tang, Z. Mao, P. Yang, B. Wang, J. Cheng, D. Yao, G. Zhang, and M. Wang, Nature, **621**, 493-498 (2023).

[13] M. Hepting, D. Li, C. J. Jia, H. Lu, E. Paris, Y. Tseng, X. Feng, M. Osada, E. Been, Y. Hikita, Y. D. Chuang, Z. Hussain, K. J. Zhou, A. Nag, M. Garcia-Fernandez, M. Rossi, H. Y. Huang, D. J. Huang, Z. X. Shen, T. Schmitt, H. Y. Hwang, B. Moritz, J. Zaanen, T. P. Devereaux, and W. S. Lee, Nat. Mater. **19**, 381-385 (2020).

[14] Z. Chen, M. Osada, D. Li, E.M. Been, S.-D. Chen, M. Hashimoto, D. Lu, S.-K. Mo, K. Lee, B. Y. Wang, F. Rodolakis, J. L. McChesney, C. Jia, B. Moritz, T. P. Devereaux, H. Y. Hwang, and Z. Shen, Matter, **5**, 1806-1815 (2022).

[15] M. Jiang, M. Berciu, G. A. Sawatzky, Phys. Rev. Lett. **124**, 207004 (2020).

[16] H. Lu, M. Rossi, A. Nag, M. Osada, D. Li, K. Lee, B. Wang, M. Garcia-Fernandez, S. Agrestini, Z. Shen, E. M. Been, B. Moritz, T. P. Devereaux, J. Zaanen, H. Y. Hwang, K.-J. Zhou, and W. S. Lee, Science, **373**, 213 (2021).

[17] X. Zhou, X. Zhang, J. Yi, P. Qin, Z. Feng, P. Jiang, Z. Zhong, H. Yan, X. Wang, H. Chen, H. Wu, X. Zhang, Z. Meng, X. Yu, M. B. H. Breese, J. Cao, J. Wang, C. Jiang, and Z. Liu, Adv. Mater. **34**, 2106117 (2022).

[18] J. Fowlie, M. Hadjimichael, M.M. Martins, D. Li, M. Osada, B.Y. Wang, K. Lee, Y. Lee, Z. Salman, T. Prokscha, J.-M. Triscone, H. Y. Hwang, and A. Suter, Nat. Phys. **18**, 1043 (2022).

[19] L. E. Chow, S. K. Sudheesh, Z. Luo, P. Nandi, T. Heil, J. Deuschle, S. Zeng, Z. Zhang, S. Prakash, X. Du, Z. S. Lim, P. A. van Aken, E. E. M. Chia, and A. Ariando, Preprint at https://arxiv.org/abs/2201.10038 (2022).

[20] S. P. Harvey, B. Y. Wang, J. Fowlie, M. Osada, K. Lee, Y. Lee, D. Li, H.Y. Hwang, Preprint at https://arxiv.org/abs/2201.12971 (2022).

[21] B. Cheng, D. Cheng, K. Lee, L. Luo, Z. Chen, Y. Lee, B.Y. Wang, M. Mootz, I.E. Perakis, Z.-X. Shen, H. Y. Hwang, and J. Wang, Nat. Mater. https://doi.org/10.1038/s41563-023-01766-z (2024).

[22] Z. Wang, G.-M. Zhang, Y.-f. Yang, F.-C. Zhang, Phys. Rev. B, **102**, 220501 (2020).

[23] C. C. Tam, J. Choi, X. Ding, S. Agrestini, A. Nag, M. Wu, B. Huang, H. Luo, P. Gao, M. García-Fernández, L. Qiao, and K. J. Zhou, Nat. Mater. **21**, 1116 (2022).

[24] G. Krieger, L. Martinelli, S. Zeng, L. Chow, K. Kummer, R. Arpaia, M.M. Sala, N.B. Brookes, A. Ariando, N. Viart, M. Salluzzo, G. Ghiringhelli, and D. Preziosi, Phys. Rev. Lett. **129**, 027002 (2022).

[25] M. Rossi, M. Osada, J. Choi, S. Agrestini, D. Jost, Y. Lee, H. Lu, B. Y. Wang, K. Lee, A. Nag, Y.-D. Chuang, C.-T. Kuo, S.-J. Lee, B. Moritz, T. P. Devereaux, Z.-X. Shen, J.-S. Lee, K.-J. Zhou, H. Y. Hwang, amd W.-S. Lee, Nat. Phys. **18**, 869 (2022).

[26] C. Parzyck, N. Gupta, Y. Wu, V. Anil, L. Bhatt, M. Bouliane, R. Gong, B. Gregory, A. Luo, R. Sutarto, F. He, Y.-D. Chuang, T. Zhou, G. Herranz, L. F. Kourkoutis, A. Singer, D. G. Schlom, D. G. Hawthorn, and K. M. Shen, Nat. Mater. **23**, 486 (2024).

[27] Q. Li, C. He, J. Si, X. Zhu, Y. Zhang, H.-H. Wen, Commun. Mater. **1**, 16 (2020).

[28] B.-X. Wang, H. Zheng, E. Krivyakina, O. Chmaissem, P. P. Lopes, J. W. Lynn, L. C. Gallington, Y. Ren, S. Rosenkranz, J. Mitchell, and D. Phelan, Phys. Rev. Mater. **4**, 084409 (2020).

[29] K. Lee, B. H. Goodge, D. Li, M. Osada, B. Y. Wang, Y. Cui, L. F. Kourkoutis, H. Y. Hwang, APL Mater. **8**, 041107 (2020).

[30] Z. Meng, H. Yan, P. Qin, X. Zhou, X. Wang, H. Chen, L. Liu, Z. Liu, Adv. Funct. Mater. **33**, 2305225 (2023).

[31] X. Ding, C. C. Tam, X. Sui, Y. Zhao, M. Xu, J. Choi, H. Leng, J. Zhang, M. Wu, H. Xiao, X. Zu, M. Garcia-Fernandez, S. Agrestini, X. Wu, Q. Wang, P. Gao, S. Li, B. Huang, K.-J. Zhou and L. Qiao, Nature, **615**, 50 (2023).

[32] L. Si, P. Worm, D. Chen, and K. Held, Phys. Rev. Lett. **124**, 166402 (2020).

[33] C. Qin, M. Jiang, and L. Si, Phys. Rev. B **108**, 155147 (2023).

[34] S. Di Cataldo, P. Worm, L. Si, and K. Held, Phys. Rev. B **108**, 174512 (2023).

[35] W. Wei, D. Vu, Z. Zhang, F. J. Walker, and C. H. Ahn, Sci. Adv. **9**, eadh3327 (2023).

[36] See Supplemental Material at http://link.aps.org/ for the details of Methods and Figures S1-S5.

[37] T. Onozuka, A. Chikamatsu, T. Katayama, T. Fukumura, and T. Hasegawa, Dalton Trans. **45**, 12114 (2016).

[38] P. Puphal, V. Pomjakushin, R. A. Ortiz, S. Hammoud, M. Isobe, B. Keimer, M. Hepting, Front. Phys. **10**, 115 (2022).

[39] T. Katayama, A. Chikamatsu, K. Yamada, K. Shigematsu, T. Onozuka, M. Minohara, H. Kumigashira, E. Ikenaga, and T. Hasegawa, J. Appl. Phys., **120**, 085305 (2016).

[40] M. Rossi, H. Lu, A. Nag, D. Li, M. Osada, K. Lee, B.Y. Wang, S. Agrestini, M. Garcia-Fernandez, J. Kas, Y.-D. Chuang, Z. X. Shen, H. Y. Hwang, B. Moritz, K.-J. Zhou, T. P. Devereaux, and W. S. Lee, Phys. Rev. B, **104**, L220505 (2021).

[41] Y. Nomura, and R. Arita, Rep. Prog. Phys. **85**, 052501 (2022).

[42] M. Kitatani, L. Si, O. Janson, R. Arita, Z. Zhong, and K. Held, npj Quantum Mater. **5**, 59 (2020).

[43] K. Han, M. Xie, Y. Mei, R. Lin, L. Xu, P. Chen, P. Yin, S. Zeng, B. Ge, A. Ariando, D. Song, X. R. Wang, W. Wu, and Z. Huang, Appl. Phys. Lett. **123**, 182601 (2023).

[44] R. He, P. Jiang, Y. Lu, Y. Song, M. Chen, M. Jin, L. Shui, and Z. Zhong, Phys. Rev. B, **102**, 035118 (2020).

[45] F. Bernardini, and A. Cano, J. Phys. Mater. **3**, 03LT01 (2020).

[46] B. H. Goodge, B. Geisler, K. Lee, M. Osada, B.Y. Wang, D. Li, H.Y. Hwang, R. Pentcheva, L.F. Kourkoutis, Nat. Mater. **22**, 466-473 (2023).

[47] A. S. Botana, and M. R. Norman, Phys. Rev. X **10,** 011024 (2020).

[48] S. Zeng, X. Yin, C. Li, L. Chow, C. Tang, K. Han, Z. Huang, Y. Cao, D. Wan, Z. Zhang, Z. S. Lim, C. Z. Diao, P. Yang, A. T. S. Wee, S. J. Pennycook and A. Ariando, Nat. Commun. **13**, 743 (2022).

[49] P. Puphal, Y.-M. Wu, K. Fürsich, H. Lee, M. Pakdaman, J. A. Bruin, J. Nuss, Y. E. Suyolcu, P. A. van Aken, B. Keimer, M. Isobe, and M. Hepting, Sci. Adv. **7**, eabl8091 (2021).

Figures and Captions

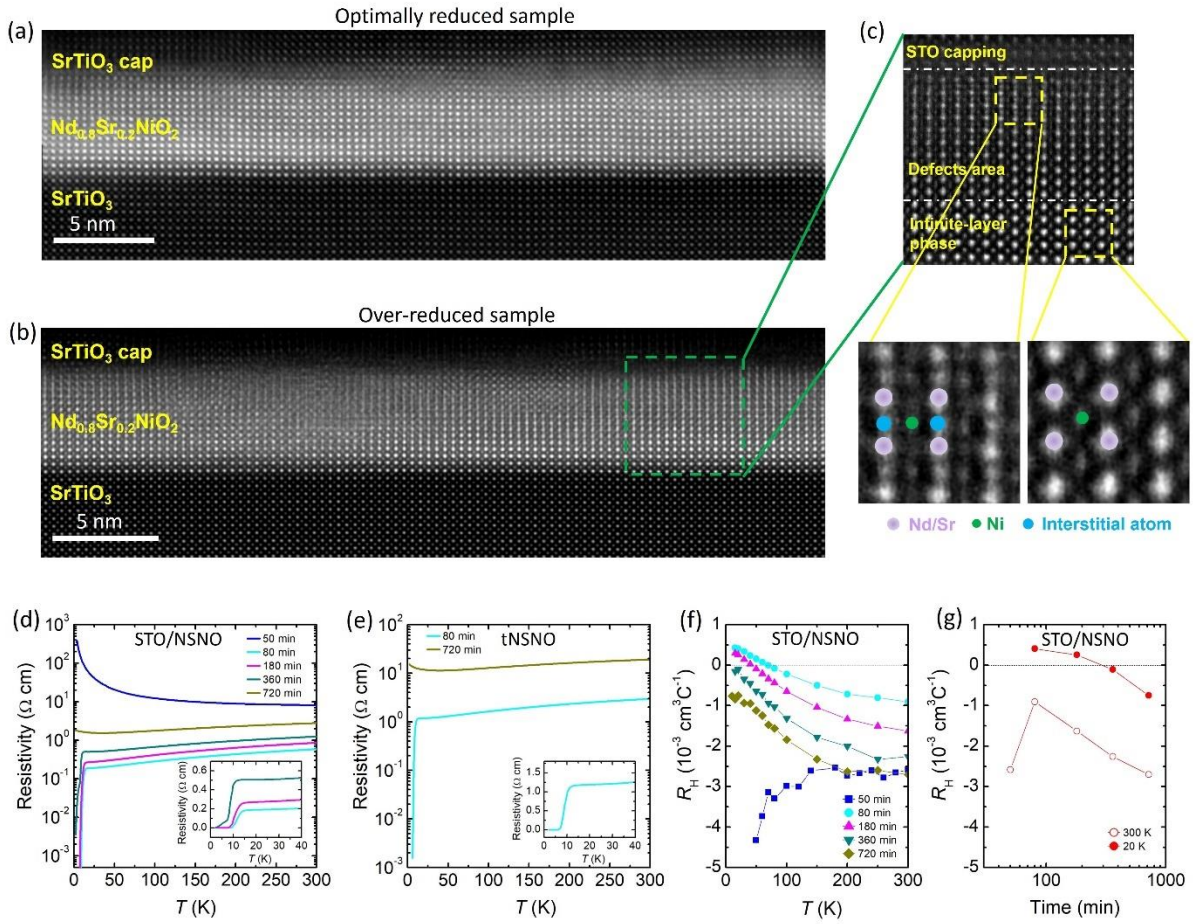

FIG. 1. Topotactic reduction effect on the crystalline structure and electrical transport property. (a),(b) HAADF-STEM cross-sectional images of STO/NSNO at the optimally reduced duration of 80 mins and over-reduced duration of 720 mins, respectively. (c) The magnified view of the region marked by the green dashed box (top) and regions marked by the yellow dashed box (bottom) for the over-reduced sample. (d),(e) The logarithmic-scale resistivity *versus* temperature (ρ-T) curves of STO/NSNO and tNSNO, respectively. The insets show the zoomed-in and linear-scale ρ-T curves of the superconducting samples. (f) The temperature dependence of normal-state Hall coefficients R_H of STO/NSNO. (g) The R_H of STO/NSNO at 300 and 20 K as a function of reduction time.

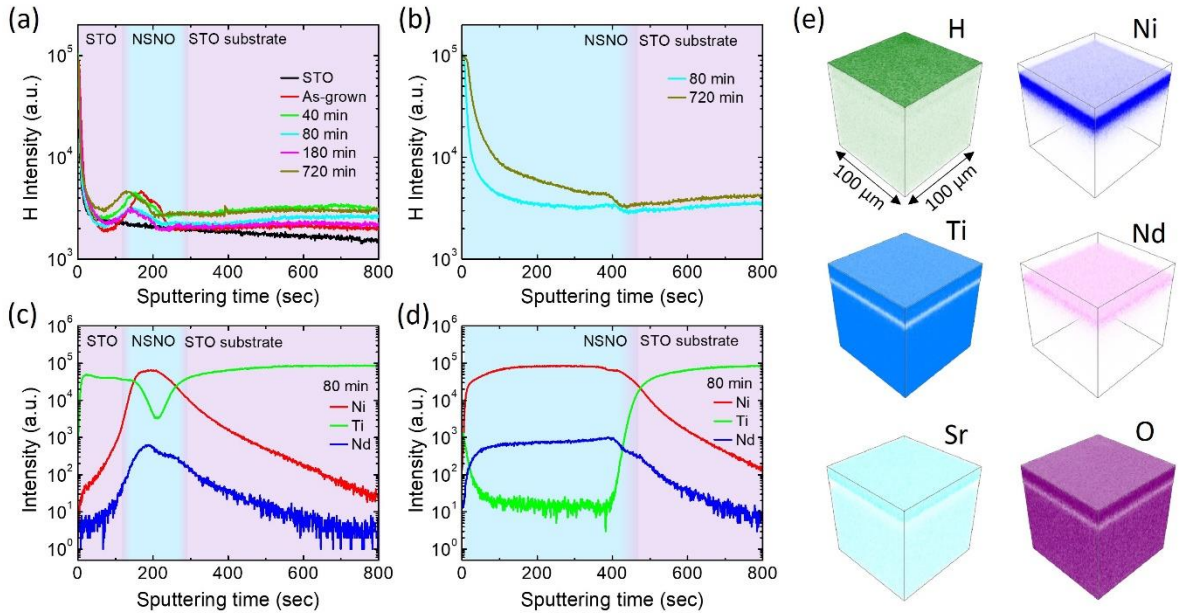

FIG. 2. TOF-SIMS element profiles and 3D mapping. (a),(b) SIMS signals of H profile for STO/NSNO and tNSNO, respectively. (c),(d) Signals of Ni, Ti and Nd profile for STO/NSNO and tNSNO, respectively, at reduction time of 80 mins. (e) 3D mappings of H, Ni, Ti, Nd, Sr and O elements for the STO/NSNO reduced for 80 mins. The elements profiles are collected from the negative ions H^-, Ni^-, TiO^-, NdO^-, SrO^-, O^{2-}.

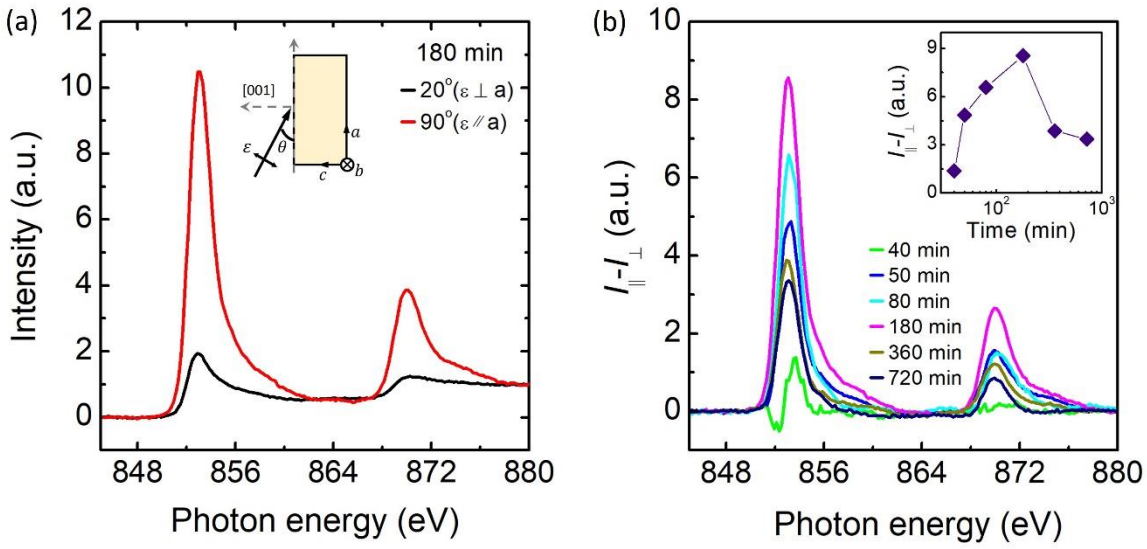

FIG. 3. Reduction effect on XAS. (a) Ni $L_{2,3}$ edge XAS of STO/NSNO at reduction time of 180 mins. The inset shows the direction of photon polarization ε and incident angle. (b) The intensity difference (XLD, $\Delta I = I(\varepsilon // a) - I(\varepsilon \perp a)$) of STO/NSNO reduced at different duration. The inset is Ni-L_3 peak intensity difference versus reduction time.

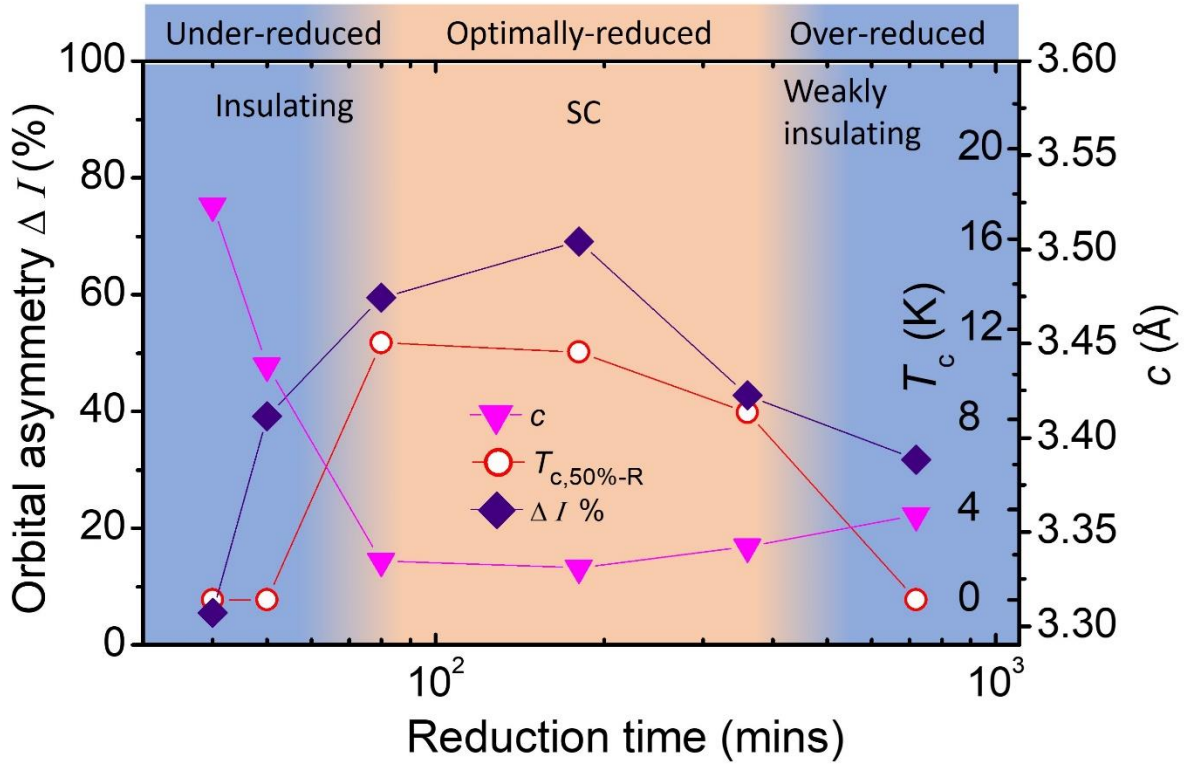

FIG. 4. Reduction phase diagram of infinite-layer nickelate. The XAS spectral asymmetry at Ni L_3 peak, $\Delta I\% = [I(\varepsilon /\!/ a) - I(\varepsilon \perp a)] / [I(\varepsilon /\!/ a) + I(\varepsilon \perp a)]$, the superconducting critical temperature T_c, and the c-axis lattice constant c, versus reduction duration for STO/NSNO. The $T_{c\ 50\%\text{-}R}$ is defined to be the temperature at which the resistivity drops to 50 % of the value at 20 K (the onset of the superconductivity).